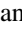
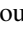














# Resolving Clumpy versus Extended Ly $\alpha$ in Strongly Lensed, High-redshift Ly $\alpha$ Emitters

Alexander Navarre<sup>1</sup> , Gourav Khullar<sup>2</sup> , Matthew B. Bayliss<sup>1</sup> , Håkon Dahle<sup>3</sup> , Michael Florian<sup>4</sup> , Michael Gladders<sup>5</sup> ,  
Keunho J. Kim<sup>1</sup> , M. Riley Owens<sup>1</sup> , Jane Rigby<sup>6</sup> , Joshua Roberson<sup>1</sup> , Keren Sharon<sup>7</sup> , Takatoshi Shibuya<sup>8</sup>, and  
Ryan Walker<sup>7</sup> 

<sup>1</sup> Department of Physics, University of Cincinnati, Cincinnati, OH 45221, USA

<sup>2</sup> Department of Physics and Astronomy and PITT PACC, University of Pittsburgh, Pittsburgh, PA 15260, USA

<sup>3</sup> Institute of Theoretical Astrophysics, University of Oslo, Oslo, Norway

<sup>4</sup> Steward Observatory, University of Arizona, Tucson, AZ 85719, USA

<sup>5</sup> Department of Astronomy and Astrophysics, University of Chicago, Chicago, IL 60637, USA

<sup>6</sup> NASA Goddard Space Flight Center, Greenbelt, MD 20771, USA

<sup>7</sup> Department of Astronomy, University of Michigan, Ann Arbor, MI 48109, USA

<sup>8</sup> Kitami Institute of Technology, Kitami, Hokkaido, Japan

Received 2023 July 25; revised 2023 November 26; accepted 2023 November 27; published 2024 February 19

## Abstract

We present six strongly gravitationally lensed Ly $\alpha$  emitters (LAEs) at  $z \sim 4\text{--}5$  with Hubble Space Telescope (HST) narrowband imaging isolating Ly $\alpha$ . Through complex radiative transfer Ly $\alpha$  encodes information about the spatial distribution and kinematics of the neutral hydrogen upon which it scatters. We investigate the galaxy properties and Ly $\alpha$  morphologies of our sample. Many previous studies of high-redshift LAEs have been limited in Ly $\alpha$  spatial resolution. In this work we take advantage of high-resolution Ly $\alpha$  imaging boosted by lensing magnification, allowing us to probe subgalactic scales that are otherwise inaccessible at these redshifts. We use broadband imaging from HST (rest-frame UV) and Spitzer (rest-frame optical) in spectral energy distribution fitting, providing estimates of the stellar masses ( $\sim 10^8\text{--}10^9 M_\odot$ ), stellar population ages ( $t_{50} < 40$  Myr), and amounts of dust ( $A_V \sim 0.1\text{--}0.6$ , statistically consistent with zero). We employ nonparametric star formation histories to probe the young stellar populations which create the Ly $\alpha$ . We also examine the offsets between the Ly $\alpha$  and stellar continuum, finding small upper limits of offsets ( $< 0''.1$ ) consistent with studies of low-redshift LAEs, indicating our galaxies are not interacting or merging. Finally, we find a bimodality in our sample's Ly $\alpha$  morphologies: clumpy and extended. We find a suggestive trend: our LAEs with clumpy Ly $\alpha$  are generally younger than the LAEs with extended Ly $\alpha$ , suggesting a possible correlation with age.

*Unified Astronomy Thesaurus concepts:* Lyman-alpha galaxies (978); Strong gravitational lensing (1643); High-redshift galaxies (734); Spectral energy distribution (2129)

## 1. Introduction

### 1.1. Ly $\alpha$ and LAEs

Ly $\alpha$  is emitted from the atomic transition  $n = 2$  to  $n = 1$  of hydrogen. It is hydrogen's brightest recombination line, and abundantly appears in many young, star-forming galaxies. Due to its complex interactions with neutral hydrogen gas, Ly $\alpha$  is an important tool for studying the properties of young stellar populations. It traces recent star formation and carries information about the morphology and kinematics of neutral hydrogen gas.

Young, massive stars in regions of neutral hydrogen (HI regions) produce Ly $\alpha$  in abundance. To first order, these stars ionize their surroundings, creating regions of ionized hydrogen (HII regions). At the boundaries of HI and HII regions the ionization rate and recombination rate balance out. As recombination happens the electron cascades down to the ground state, with a likelihood of  $\approx 68\%$  to create an Ly $\alpha$  photon (this assumes Case B recombination and a temperature of  $10^4$  K; see Dijkstra 2017). This can be thought of as an effective conversion factor which locally converts ionizing photons into Ly $\alpha$  photons. Although, it is important to note that

other mechanisms, such as collisional excitation, also create Ly $\alpha$  photons within these environments. Significant Ly $\alpha$  emission traces the formation of these stars over cosmological timescales, implying that the host galaxy is young. Similarly, it implies that there is not an abundance of dust in the host galaxy, which would otherwise attenuate the Ly $\alpha$  flux (Scarlata et al. 2009; Henry et al. 2015; Saldana-Lopez et al. 2023).

A class of galaxies exists which emit significant amounts of Ly $\alpha$  (Cowie & Hu 1998). These galaxies are called Ly $\alpha$  emitters (LAEs), and are typically classified as having some minimum equivalent width (EW). This minimum EW is often related to the detection thresholds of the narrowband imaging surveys used to identify samples of LAEs. There is no obvious consensus in the literature on a single Ly $\alpha$  EW threshold, though  $EW \gtrsim 20 \text{ \AA}$  is perhaps the most common. The objects in our sample all have Ly $\alpha$  EW  $> 15 \text{ \AA}$ , which is very similar (albeit slightly below) the most common literature selection criteria. LAEs are thought to be young and actively star forming with low to moderate dust content (Gronwall et al. 2007; Finkelstein et al. 2008; Ouchi et al. 2008).

### 1.2. Ly $\alpha$ Radiative Transfer

There is a complex set of radiative transfer processes that Ly $\alpha$  photons can undergo with neutral hydrogen (Dijkstra 2017). The simplest conceptual path for an Ly $\alpha$  photon to take is direct escape from the galaxy after its initial



Original content from this work may be used under the terms of the [Creative Commons Attribution 4.0 licence](https://creativecommons.org/licenses/by/4.0/). Any further distribution of this work must maintain attribution to the author(s) and the title of the work, journal citation and DOI.

creation. However, we see in many star-forming galaxies that the Ly $\alpha$  emission is spatially extended and/or offset from the associated stellar continuum (Östlin et al. 2009; Hayes et al. 2013). This happens because the photons interacted with neutral hydrogen atoms in between their initial creation and escape. Neutral hydrogen interacting with an Ly $\alpha$  photon will absorb and reemit the photon in a random direction, effectively scattering it. This scattering process can happen many times before the Ly $\alpha$  photon is able to escape the galaxy, allowing the Ly $\alpha$  photon to travel far from its original creation site. This leads to Ly $\alpha$  emission that is spatially broader than the stellar continuum.

### 1.3. High-redshift LAEs

LAEs are typical targets for high-redshift galaxy studies because of their excess brightness in narrowband imaging. Many LAEs have been found at low (Deharveng et al. 2008; Cowie et al. 2011; Östlin et al. 2014) and high redshifts (Cowie & Hu 1998; Rhoads et al. 2000; Yamada et al. 2005; Ouchi et al. 2008; Marques-Chaves et al. 2017; Mukae et al. 2020; Kikuta et al. 2023), suggesting that they are galaxies in a specific stage of evolution, thought to be the progenitors of Milky Way–type galaxies in the local Universe (Ono et al. 2010; Dressler et al. 2011; Guaita et al. 2011). However, the astrophysical mechanisms that differentiate this stage are not well understood at high redshifts. For example, narrowband Ly $\alpha$  imaging of LAEs shows heterogeneous morphologies. They range from clumpy (scale radii  $\sim 0.5$  kpc; Bond et al. 2010; Finkelstein et al. 2011) and comparable to stellar continuum sizes, to moderately extended (scale radius  $\sim 2$  kpc; Jung et al. 2023), to significantly extended (scale radii  $\sim 80$  kpc; Steidel et al. 2011).

Recent studies with JWST and MUSE have shown the importance of faint LAEs to cosmic reionization. Thai et al. (2023) find an abundance of faint LAEs at high redshift, and Atek et al. (2023) find that faint high-redshift LAEs have very high ionizing photon production efficiencies. This suggests that LAEs contribute more than previously thought to cosmic reionization. Witstok et al. (2024) find that their sample of spectroscopically confirmed LAEs at  $z > 7$  are alone not sufficient to produce the ionized bubble sizes inferred from their spectra. They suggest that ultrafaint ( $M_{UV} \gtrsim -18$ ) LAEs likely play an important role in carving out these bubbles. Herrero Alonso et al. (2023) find that undetected (presumably faint) LAEs could dominate excess surface brightness seen at large scales in Ly $\alpha$  halos. Magnification from gravitational lensing will be an essential tool in future studies of very faint LAEs during the epoch of reionization.

The goal of this paper is to characterize a sample of high-redshift, gravitationally lensed LAEs imaged by the Hubble Space Telescope (HST) and Spitzer. We measure their stellar masses, ages, and dust contents ( $A_V$ ), gaining context of the environments in which the Ly $\alpha$ -emitting regions exist. We also measure the Ly $\alpha$  fluxes and luminosities in both the image plane (observed, magnified) and source plane (intrinsic, demagnified). These measurements, in conjunction with previously measured Ly $\alpha$  EWs, show the strength of the Ly $\alpha$  emission.

This paper is organized as follows: in Section 2 we introduce our sample of LAEs and summarize the data used. In Section 3 we describe our methodologies and measurements. In Section 4 we analyze our measurements and discuss our findings.

Throughout this paper we assume a Lambda cold dark matter ( $\Lambda$ CDM) cosmology with  $(H_0, \Omega_m, \Omega_\Lambda) = (67.7 \text{ kms}^{-1} \text{ Mpc}^{-1}, 0.31, 0.69)$ .

## 2. Data

### 2.1. Lensed LAE Sample

We analyze a sample of six high-redshift ( $z > 4$ ) LAEs. These six lensed LAEs are in the redshift range  $4.1 < z < 5.2$ . All six have published, well-constrained strong lensing models (Rzepecki et al. 2007; Swinbank et al. 2007; Bayliss et al. 2010, 2014; Smit et al. 2017; Sharon et al. 2020), allowing for spatial analysis at resolutions otherwise inaccessible at these redshifts. Previous studies such as those of Marques-Chaves et al. (2017), Berg et al. (2018), and Erb et al. (2019) have shown the utility of lensing magnification in characterizing the properties of Ly $\alpha$ -emitting galaxies both in the image plane and source plane.

All six lensed LAEs have imaging in broadband filters from HST (rest-frame UV) and Spitzer (rest-frame optical), allowing for broad constraints on the stellar population properties in each galaxy. In this paper we present new narrowband imaging using tuneable ramp filters on HST that isolate Ly $\alpha$ . These filters allow us to measure directly the morphology and spatial extent of the Ly $\alpha$  emission. The individual sources and imaging data sets are described in more detail below. For ease of reference, the six LAEs in our sample are referred to as L1–L6, as shown in Figure 1 and Tables 1 and 2.

### 2.2. Sample Discovery and Spectroscopic Observations

The sample of strongly lensed Ly $\alpha$ -emitting galaxies are drawn from the literature. L6 was first identified in the Red-Sequence Cluster Survey (RCS; Gladders et al. 2003) as a highly extended “giant arc” around a massive galaxy cluster, RCS1 J0224-0002 (see Figure 1). It was found to have a redshift of  $z = 4.8786$  based on strong Ly $\alpha$  emission observed with the FORS2 spectrograph on the Very Large Telescope (VLT; Gladders et al. 2002). L6 has been the subject of several detailed studies using ground-based optical and near-infrared spectroscopy (Swinbank et al. 2007; Smit et al. 2017; Witstok et al. 2021). The spectra of Ly $\alpha$  seen in Figure 2 are from the VIMOS IFU observations of Swinbank et al. (2007), where the IFU covered the entire arc.

L1-5 are all located in strong lensing cluster fields found in the Sloan Digital Sky Survey (SDSS; York et al. 2000; see Figure 1). The sources were identified as  $g$ - or  $r$ -band dropout galaxies in  $gri$  imaging from the GMOS-N instrument on the Gemini-North telescope. Redshifts for all these sources were measured from strong Ly $\alpha$  emission in follow-up spectroscopy with GMOS-N (Bayliss et al. 2010, 2011, 2014). The slits in these observations covered the integrated emission from individual images of each LAE. The redshifts for all six LAEs appear in Table 1.

### 2.3. HST Narrowband Imaging

We obtained narrowband imaging isolating Ly $\alpha$  for each object in our sample taken with the narrowband ramp filters installed on HST’s Advanced Camera for Surveys (ACS). These reduced data are available on the Harvard Dataverse: doi:10.7910/DVN/9Q0YYW (Navarre 2023a). These filters are tunable, allowing for coverage of precise wavelength

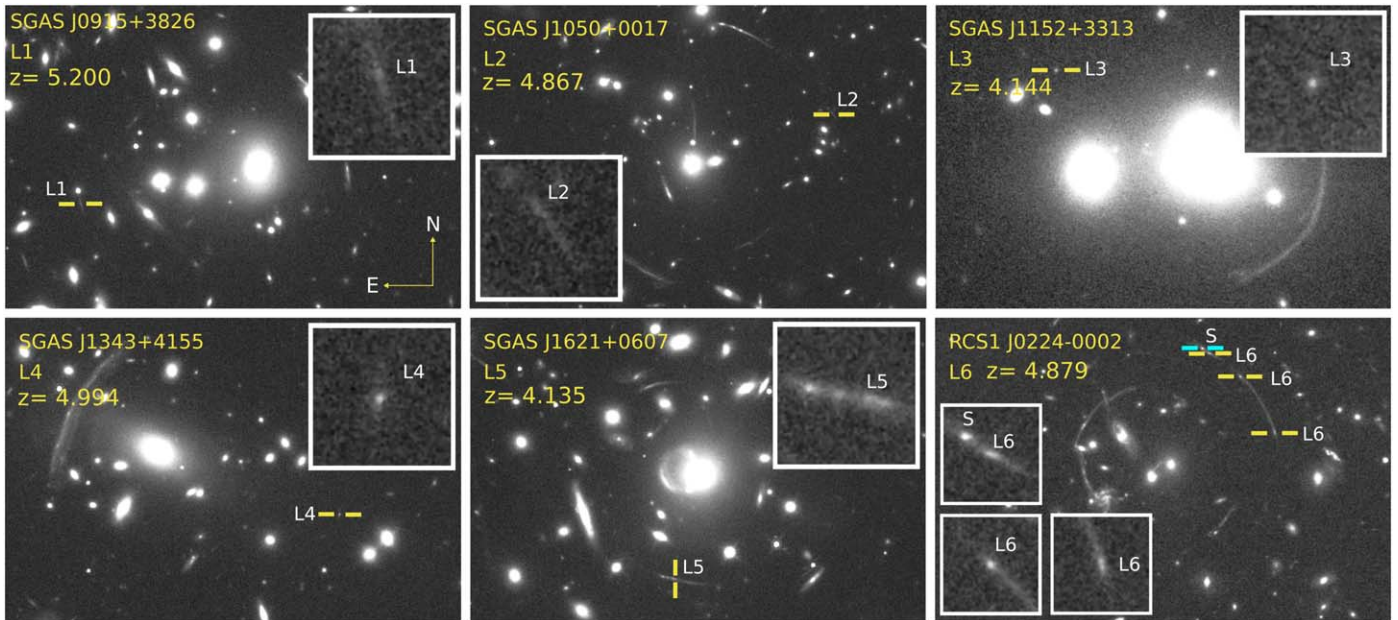


**Figure 1.** The LAE sample and lensing galaxy clusters. In the cluster view we show F160W (F814W for L6) with the LAEs located by sets of yellow bars. In the postage stamps, close-up views of the LAEs are shown in the bluest available filter redward of Ly $\alpha$  that does not contain Ly $\alpha$ . These filters are reported in Table 6 and capture light from the stellar continuum. L6 contains three bright, separated images. A bright galaxy is seen projected onto L6, which we label S and indicate with a set of cyan bars. This galaxy is not gravitationally lensed nor part of L6, but is instead a foreground  $z = 3.66$  galaxy (identified by Swinbank et al. 2007) that serendipitously appears to be part of the arc.

ranges. We obtained these data as part of HST Guest Observer (GO) program #13639 (PI: Bayliss). Each ramp filter provides an image with a narrow bandwidth ( $\Delta\lambda/\lambda \simeq 2\%$ ) over a field of view covering approximately  $\approx 40'' \times 60''$  on the sky. Each source received between one and three orbits of ramp filter observations ( $\sim 2400\text{--}7800$  s total integration time). We list the ramp filter used, the tuned central wavelength, and exposure time for each lensed LAE in Table 3. Figure 2 shows the spectra of all six lensed LAEs centered on Ly $\alpha$  with the transmission curves of the ramp filters used to isolate Ly $\alpha$  for each source. We reduced the ACS ramp filter data following standard procedures using Drizzlepac<sup>9</sup> (Gonzaga et al. 2012). We drizzled the exposures taken in each filter using the `astrodrizzle` routine with a Gaussian kernel and a drop size of `final_pixfrac=0.8`. We combined them to a common world coordinate system (WCS) using `tweakreg` and `tweakback`, and coadded them with `astrodrizzle` onto a common reference grid with north up and a pixel scale of  $0''.03 \text{ pixel}^{-1}$ . The final reduced narrowband images for each LAE are background limited.

#### 2.4. Broadband Imaging

We also analyze broadband imaging of each of our lensed LAEs from several different observatories, spanning the optical through infrared (IR). For L1 and L4 we use  $i$ - and  $z$ -band magnitudes measured with the GMOS-N instrument on the Gemini-North telescope and published by Bayliss et al. (2010). We measure additional broadband imaging photometry from HST and Spitzer data for all six lensed LAEs.

#### 2.4.1. HST

Five of our lensed LAEs—L1 through L5—were imaged with the Wide Field Camera 3 (WFC3) on HST using both the IR and UVIS channels as a part of HST-GO program #13003 (PI: Gladders). In short, each field was observed in two UVIS broadband filters—one of [F814W, F775W, F606W], and one of [F475W, F390W]—and in two IR broadband filter—F160W and one of [F125W, F110W, F105W]. L4 is a slight exception, as it has UVIS imaging only in F390W, as well as imaging from HST’s Wide Field Planetary Camera 2 (WFPC2) in F606W and F814W that was taken as a part of HST-GO program #11974 (PI: Allam). All of these observations are described in Sharon et al. (2020), and we use the same reductions described there.

L6 has HST imaging from several different programs, all of which we incorporate into our analysis. The available data include WFPC2/F814W (13,200 s) and WFPC2/F606W (6600 s) obtained with GO #9135 (PI: Gladders); ACS/F850LP (1949 s) obtained with GO #13639 (PI: Bayliss); and ACS/F814W (8046 s), WFC3-IR/F125W (12486 s), and WFC3-IR/F160W (15369 s) with GO #14497 (PI: Smit). We reduced these data using the same procedure that was applied to the ACS ramp filter data described above. For a more detailed description of the reduction methods see Sharon et al. (2020).

The available broadband data (Sharon 2022) allow us to fit spectral energy distributions (SEDs) with multiple points over a broad wavelength range for our entire sample, always with at least two HST broadband filters that sample the stellar continuum emission redward (and uncontaminated by) Ly $\alpha$ .

#### 2.4.2. Spitzer

Our lensed LAE sample has rest-frame optical broadband imaging available from observations taken with the Infrared

<sup>9</sup> <http://www.stsci.edu/scientific-community/software/drizzlepac.html>



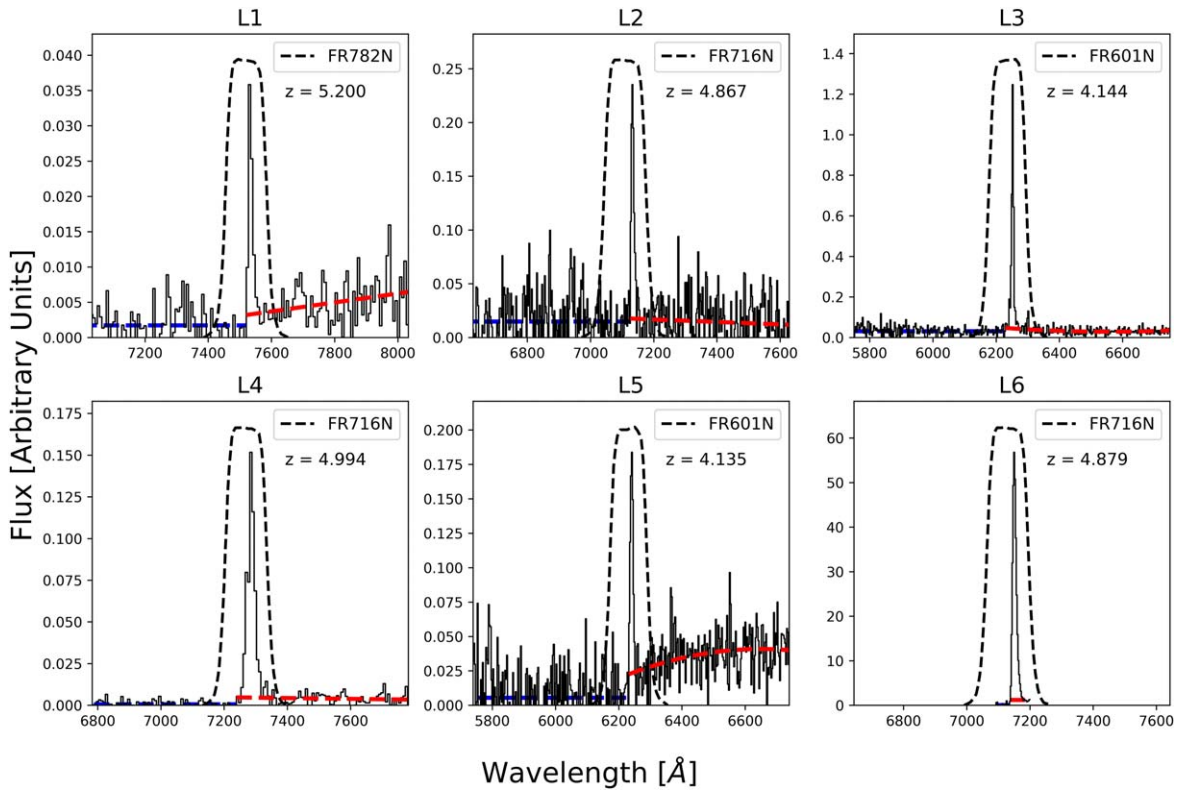


**Figure 2.** GMOS (L1–L5) and VIMOS IFU (L6) spectra of the LAE sample centered on  $\text{Ly}\alpha$ . The dashed black curve represents the throughput of the ramp filter used to capture  $\text{Ly}\alpha$ . The dashed red and blue curves represent fits to the continuum levels redward and blueward of  $\text{Ly}\alpha$ , respectively. When calculating the  $\text{Ly}\alpha$  fluxes and luminosities we include a multiplicative factor accounting for the fraction of light in the narrowband image coming directly from the  $\text{Ly}\alpha$  line. The ramp filter properties can be found in Table 3.

**Table 1**  
Positions and Redshifts of the Lensed LAEs and Lensing Clusters

Identifier	Lensing Cluster	Cluster Redshift	LAE Redshift	Cluster R.A.	Cluster Decl.	LAE R.A.	LAE Decl.
L1a	SGAS J091541+382655	0.396	5.200	09:15:39	+38:26:59	09:15:41.0	+38:26:53.2
L1b	...	...	...	...	...	09:15:41.0	+38:26:52.3
L2a	SGAS J105038+001715	0.593	4.867	10:50:40	+00:17:07	10:50:38.3	+00:17:14.9
L2b	...	...	...	...	...	10:50:38.4	+00:17:15.2
L3	SGAS J115201+331347	0.517	4.144	11:52:00	+09:30:15	11:52:01.0	+33:13:48.2
L4	SGAS J134331+415455	0.418	4.994	13:43:33	+41:55:04	13:43:30.7	+41:54:55.1
L5	SGAS J162132+060705	0.343	4.135	16:21:32	+06:07:20	16:21:32.6	+06:07:05.6
L6'	RCS1 J022434-000220	0.773	4.879	02:24:34	-00:02:31	02:24:33.8	-00:02:17.8
L6''	...	...	...	...	...	02:24:33.6	-00:02:20.5
L6'''	...	...	...	...	...	02:24:33.3	-00:02:26.9

**Note.** Lowercase letters denote bright regions inside a single image, while apostrophes denote different images of the same bright region. See Section 3.4 and Figure 3 for our justification for analyzing our LAEs in this manner. Additionally, we investigate only the brightest and/or most isolated images in each case. We refer the reader to Gladders et al. (2002), Sharon et al. (2020) for information on the other lensed images.

Array Camera (IRAC) on the Spitzer Space Telescope. These reduced data are available on the Harvard Dataverse: doi:10.7910/DVN/JSVGM8 (Navarre 2023b). For sources L1–L5 we have IRAC imaging in Channel 1 (Ch1;  $\sim 3.6 \mu\text{m}$ ) and Channel 2 (Ch2;  $\sim 4.5 \mu\text{m}$ ) taken as a part of programs #60158 (PI: Gladders), #70154 (PI: Gladders), and #90232 (PI: Rigby). For L6 we have IRAC imaging in Ch1, Ch2, Channel 3 (Ch3;  $\sim 5.8 \mu\text{m}$ ), and Channel 4 (Ch4;  $\sim 8 \mu\text{m}$ ), taken as a part of program #20754 (PI: Ellingson). Ultimately we only use the Ch1 and Ch2 data of L6 in our analysis because the combination of larger IRAC point-spread functions

(PSF) and higher backgrounds in Ch3 and Ch4 prevent us from meaningfully constraining the flux in those bands. The L6 Spitzer imaging was reduced with the same procedure as described in Section 3.2 of Florian et al. (2021) with AOR 15102976. The Spitzer data sample the rest-frame  $\sim 6000\text{--}9000 \text{ \AA}$  spectra of our lensed sources.

To correct the small coordinate offset ( $\sim 1''$ ) between the HST and Spitzer data, we used Source Extractor (Bertin & Arnouts 1996) catalogs of the HST and Spitzer imaging to match the positions of bright objects in the fields, and registered the data set onto the same WCS reference frame.

**Table 2**  
Overview of Our Sample’s UV and Ly $\alpha$  Properties

ID	Ly $\alpha$ EW (Å)	Observed			Magnification Factor $\mu$	Intrinsic		
		UV $M_{1500}$	Ly $\alpha$ Flux ( $\times 10^{-18}$ )	Ly $\alpha$ Luminosity ( $\times 10^{41}$ )		UV $M_{1500}$	Ly $\alpha$ Flux ( $\times 10^{-18}$ )	Ly $\alpha$ Luminosity ( $\times 10^{41}$ )
L1	25	−25.1	$17.9 \pm 7.6$	$53.3 \pm 22.7$	$50 \pm 17$	$-20.9 \pm 0.4$	$0.4 \pm 0.2$	$1.1 \pm 0.6$
L2	61	−24.0	$5.5 \pm 0.9$	$13.9 \pm 2.3$	$12.2 \pm 0.7$	$-21.3 \pm 0.06$	$0.4 \pm 0.1$	$1.1 \pm 0.2$
L3	65	−23.4	$141.3 \pm 1.3$	$247.0 \pm 2.4$	$72.4 \pm 9.8$	$-18.7 \pm 0.1$	$2.0 \pm 0.3$	$3.4 \pm 0.5$
L4	122	−24.0	$90.2 \pm 2.0$	$244.5 \pm 5.6$	$13.0 \pm 0.1$	$-21.2 \pm 0.01$	$6.9 \pm 0.2$	$18.8 \pm 0.5$
L5	15	−25.9	$29.5 \pm 2.0$	$51.3 \pm 3.5$	$46.1 \pm 2.7$	$-21.7 \pm 0.06$	$0.6 \pm 0.1$	$1.1 \pm 0.1$
L6	120	−25.7	$24.5 \pm 2.3$	$62.9 \pm 5.9$	$17.2 \pm 16.0$	$-22.6 \pm 1.0$	$1.4 \pm 1.3$	$3.7 \pm 3.4$

**Note.** The objects’ rest-frame Ly $\alpha$  EWs are taken from Gladders et al. (2002) and Bayliss et al. (2011, 2014). The UV absolute magnitudes were calculated from our best-fit SED models. The Ly $\alpha$  fluxes and luminosities were calculated from the HST narrowband filter imaging following the methodology reported in Section 3.1. We report the flux in units of  $\text{erg s}^{-1} \text{cm}^{-2}$ . We report the luminosities in units of  $\text{erg s}^{-1}$ . The magnifications were calculated from the lens models of each system. We note that L5 has an Ly $\alpha$  EW of 15, slightly below the common Ly $\alpha$  EW threshold of 20. We include it in our sample due to its large observed Ly $\alpha$  flux and high signal-to-noise ratio.

**Table 3**  
Description of the HST Narrowband Ramp Filter Observations

ID	Ramp Filter	Ly $\alpha$ (Å)	Central $\lambda$ (Å)	Exposure Time (s)	Detection Limit ( $\times 10^{-16}$ )
L1	FR782N	7533.0	7510	7840	1.21
L2	FR716N	7158.4	7134	5060	0.25
L3	FR601N	6249.9	6235	7800	0.33
L4	FR716N	7282.7	7270	5260	0.44
L5	FR601N	6239.0	6230	7700	0.49
L6	FR716N	7142.9	7149	2400	0.53

**Note.** These filters were chosen for their ability to adjust their wavelength coverage. The central wavelengths of the ramp filters were offset to cover the Ly $\alpha$  lines seen in the associated Gemini and VLT spectra (see Figure 2). Detection limit refers to the  $1\sigma$  uncertainty in the sky background level within an aperture covering a solid angle of  $1 \text{ arcsec}^2$ . The detection limit is reported in units of  $\text{erg s}^{-1} \text{cm}^{-2} \text{arcsec}^{-2}$ .

### 3. Methodology

#### 3.1. Photometry

AB magnitudes were measured in every available broadband filter, and are shown in Table 4. The photometry was performed using elliptical apertures that match well to isophotal contours of the LAEs. We then applied PSF-dependent encircled energy (HST) and aperture correction (Spitzer) calibrations in each band to avoid aperture-based color effects. When determining the calibration values with elliptical apertures, we treated the minor axis as an effective radius. Distortion from gravitational lensing occurs along an angular path, with which we aligned the major axis of our elliptical apertures. The less distorted radial direction is thus aligned with the minor axis, and better represents the true angular size of the image.

We estimated the errors in the photometry as a combination of background noise and poisson noise. To obtain the background noise we took measurements of the blank sky nearby each LAE, masking out bright sources. The standard deviations of these pixel sets were taken as the background noise in each pixel. The total background noise was then  $\sqrt{N^*}\sigma_{\text{sky}}$ , where  $N$  is the number of pixels within the photometric aperture. The Poisson noise was calculated as

$\sqrt{N_e}$  where  $N_e$  is the (background-subtracted) number of electrons measured within the photometric aperture. These errors were summed in quadrature to obtain the total errors reported.

We report the narrowband Ly $\alpha$  fluxes and luminosities in Table 2. The Ly $\alpha$  flux density was calculated in the same manner as the broadband photometry described above. The total flux was calculated by multiplying the flux density by the bandwidth of the narrowband filter in which it was observed. We remove the continuum contribution to the narrowband flux for each object. We do this by fitting the continuum both redward and blueward of Ly $\alpha$  (see Figure 2) and using the continuum fit to compute directly the fraction of the total integrated flux in each narrowband filter that results from the continuum versus line emission. We compute the Ly $\alpha$  luminosity from the continuum-subtracted Ly $\alpha$  flux and the cosmological luminosity distance at the LAE redshift. We do not use the Ly $\alpha$  photometry in our SED modeling because Prospector does not rigorously model Ly $\alpha$  radiative transfer.

Multiple imaging refers to when one lensed object has multiple known images. For objects in our sample that were multiply imaged we analyzed only a subset, preferentially choosing the brightest and/or most isolated. The chosen images are the ones indicated by the yellow bars in Figure 1. L1, L2, L3, and L5 have multiple images, but only one was bright enough and isolated enough from other nearby bright sources. L4, while highly magnified, is not multiply imaged. L6 has three bright, isolated images. Our photometry of L6 is a combination of all its images, as they are not separable in the Spitzer imaging.

It is visually obvious from the panel containing L5 in Figure 1 that the image contains three bright regions. However, only one of these regions contains Ly $\alpha$  (the westernmost region, see Figure 3). Like L6, our photometry of L5 is a combination of all three regions because they are not separable in the Spitzer imaging. However, our offset measurements (Section 3.4) consider only the region containing Ly $\alpha$ .

Many of the LAEs in our sample have significantly brighter neighboring sources which could in principle contaminate the photometry. This is especially a concern for the Spitzer data as Spitzer pixels and PSF are large compared to the LAE sizes and the HST PSF, leading to

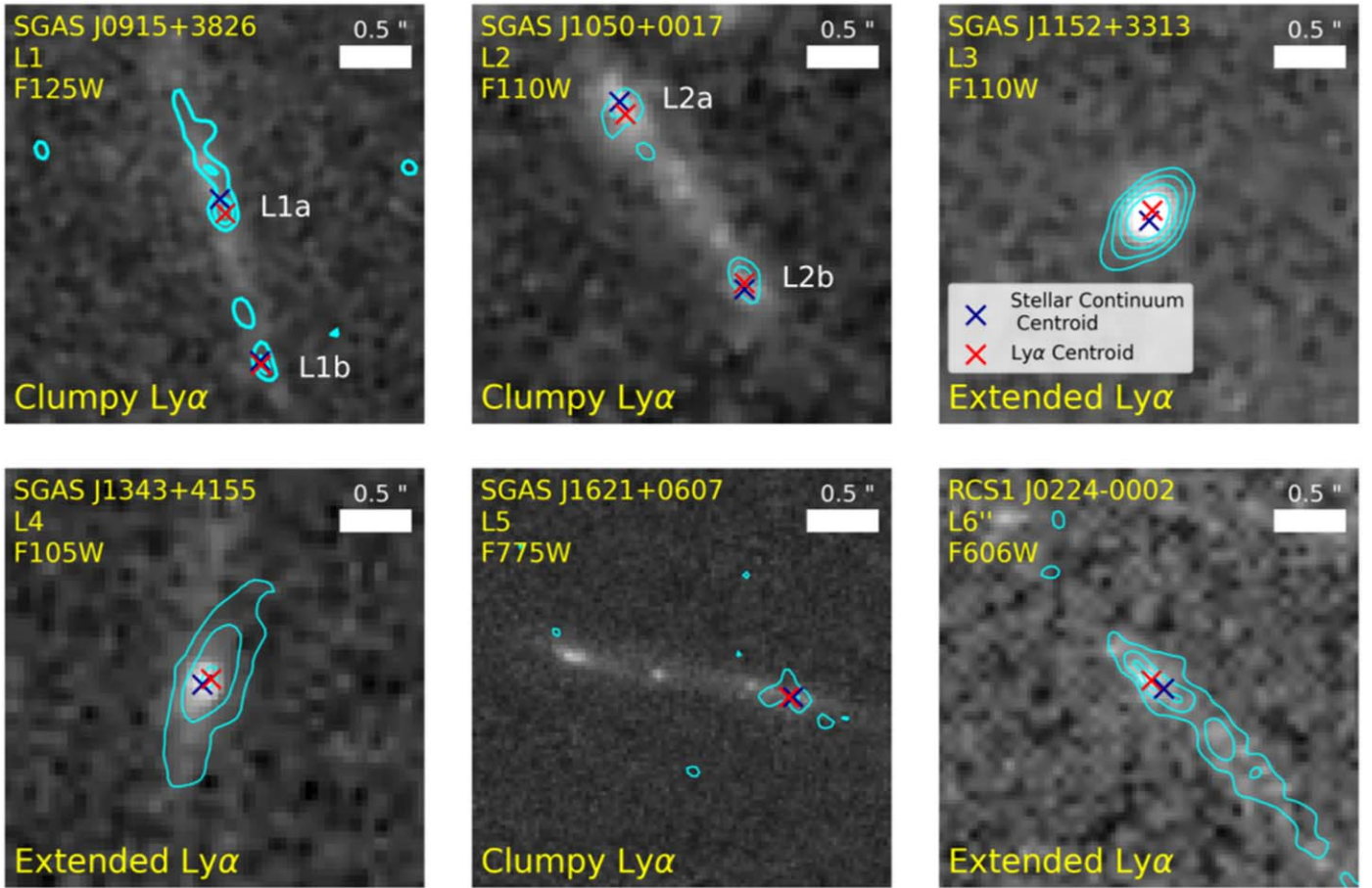


**Figure 3.** View of the LAE morphologies in the stellar continuum (grayscale) and  $\text{Ly}\alpha$  (cyan contours). The centroids of each clump are marked with blue and red Xs, corresponding with stellar continuum and  $\text{Ly}\alpha$ , respectively. We explicitly label the different bright regions found within L1 and L2 in white lettering. The sigma levels of the  $\text{Ly}\alpha$  contours are as follows: L1:[2, 3, 4], L2:[2, 3], L3:[2, 4, 8, 16], L4:[2, 4, 8], L5:[1, 2], and L6:[2, 4, 6].

**Table 4**  
Table of Broadband Photometry

Telescope	Filter	L1	L2	L3	L4	L5	L6
HST	F160W	$23.60 \pm 0.02$	$24.75 \pm 0.05$	$24.60 \pm 0.03$	$24.16 \pm 0.02$	$21.92 \pm <0.01$	$22.43 \pm 0.03$
...	F125W	$23.43 \pm 0.02$	...	...	...	...	$22.56 \pm 0.02$
...	F110W	...	$24.45 \pm 0.02$	$24.58 \pm 0.06$	...	$21.97 \pm <0.01$	...
...	F105W	...	...	...	$24.32 \pm 0.03$	...	...
HST	F850LP	...	...	...	...	...	$22.62 \pm 0.08$
...	F814W	$23.38 \pm 0.02$	...	...	$24.16 \pm 0.04$	...	$21.94 \pm 0.01$
...	F775W	...	...	...	...	$22.10 \pm 0.02$	...
...	F606W	...	$26.01 \pm 0.15$	$24.16 \pm 0.03$	$27.21 \pm 0.19$	...	$23.49 \pm 0.02$
...	F475W	...	...	$25.58 \pm 0.10$	...	...	...
...	F390W	$<7.45\text{e-}12$	$<1.64\text{e-}12$	...	$<8.08\text{e-}14$	$<1.28\text{e-}11$	...
Spitzer	Ch1	$24.32 \pm 0.97$	$23.76 \pm 0.19$	$23.75 \pm 0.62$	$23.51 \pm 0.39$	$20.77 \pm 0.02$	$21.31 \pm 0.04$
...	Ch2	...	$23.85 \pm 0.55$	$<1.80\text{e-}10$	...	$20.89 \pm 0.04$	$22.09 \pm 0.13$
Ground Based	<i>i</i> band	<b><math>23.34 \pm 0.09</math></b>	...	...	<b><math>23.78 \pm 0.18</math></b>	...	...
...	<i>z</i> band	<b><math>23.39 \pm 0.13</math></b>	...	...	<b><math>24.24 \pm 0.17</math></b>	...	...

**Note.** We report the AB magnitudes and errors used in our analysis. The italicized entries are considered nondetections, and upper limits are reported in the SDSS unit of maggies to avoid very high AB magnitudes. Maggies are a dimensionless unit defined by  $\frac{f_\nu}{3631\text{Jy}}$ . Bold entries are measurements taken from Bayliss et al. (2010). All other entries were calculated in this work.

blending of sources. To correct for this, the software GALFIT (Peng et al. 2010) was used to subtract out the bright nearby sources. The GALFIT models were Sérsics, 2D Gaussians, or a linear combination of the two. Models of the PSF were

empirically created from the available stars in each field and photometric band. The geometric models of the galaxy were convolved with the appropriate PSF model in each iteration of the GALFIT algorithm.



L6 has a bright spot initially believed to be a bright star-forming image of the LAE. However, spectral analysis by Swinbank et al. (2007) shows that it is actually a separate galaxy at a redshift of 3.66 that happens to coincide with the lensed arc. This object is labeled by the cyan bars in Figure 1, and was subtracted using GALFIT before any photometric measurements were performed. In the Spitzer data where this galaxy is indistinguishable from the LAE, we attempt to subtract it by first using GALFIT to create a model of it in F160W. We then transfer the F160W model to the Spitzer data, keeping the position and morphological parameters fixed while allowing the brightness to change.

Our GALFIT models fit the outer regions of galaxies well, but left behind residuals in the cores. However, in most cases these residuals were ignored. Through iterating GALFIT, we were able to build models where the residuals were small and spatially removed enough from our apertures. In a subset of the Spitzer imaging this was not the case, and our apertures contained imperfect residuals. To combat contamination in these cases we calculated photometry given five GALFIT models with different model parameterizations and similarly good qualities of fit, then reported the average. Particularly in L1–L4, this led to higher uncertainties than due to the sky background alone. L1–L4 are spatially compact and the most susceptible to blending with their bright neighbors. The magnitude of the GALFIT systematic uncertainties was similar to the magnitude of the uncertainty from the sky background in any particular realization. In all cases, the GALFIT residuals are believed to be a consequence of imperfect PSF modeling and/or contamination from intracluster light.

### 3.2. Stellar Population Synthesis Modeling with *Prospector*

We utilize the *Prospector* (Johnson et al. 2021) framework for Bayesian SED fitting and stellar population synthesis modeling based on the photometric and spectral measurements reported in this work. *Prospector* utilizes stellar libraries (Conroy et al. 2009; Conroy & Gunn 2010), and employs Markov Chain Monte Carlo (MCMC; Foreman-Mackey et al. 2013) to sample posterior distributions of galaxy parameter spaces. Each parameter in this multidimensional space corresponds one to one with galaxy properties such as stellar mass or  $A_V$ .

The best-fit SEDs for our sample of LAEs are shown in Figure 4. The reported properties and uncertainties are the 16th, 50th, and 84th percentiles of these distributions. These percentiles correspond to the mean and standard deviations of a Gaussian distribution. While the probability distributions sampled by *Prospector* are not necessarily Gaussian, these percentiles still provide a suitable measure of the values and uncertainties.

We ran *Prospector* with a combination of the parametric\_sfh, dust\_emission, and nebular libraries. These libraries allow us to model jointly the stellar mass, stellar metallicity, stellar population age, amount of dust, gas-phase metallicity, and ionization parameter U as free parameters. However, the constraining power of our photometry only robustly constrained the stellar mass. The amount of dust and age of each stellar population are less constrained, but are reported for context. The stellar and gas-phase metallicities and the ionization parameter U were not meaningfully constrained. Redshift was kept fixed in all cases except for L4, which had a strong  $H\alpha$  emission line on the edge of the IRAC Channel 1

transmission curve. This was inferred from the brightness of the  $Ly\alpha$  line and the  $Ly\alpha$ -based redshift. We do not have a precise measurement of the true systematic redshift, so in this case we allowed the redshift to vary over a small range calculated using Verhamme et al. (2018): an investigation into the offsets between the systematic and  $Ly\alpha$ -based redshift measurements. The extent to which  $H\alpha$  lies under the transmission curve has a large impact on the inferred properties from the fit. Allowing the redshift to vary for L4 ensures we are not biased toward only one possible set of parameters. Additionally, we chose to exclude any photometry from bands that contained  $Ly\alpha$  because *Prospector* cannot model  $Ly\alpha$  emission rigorously.

At the redshifts of our sample the HST photometry constrains the UV slope and luminosity of the young stellar populations. The Spitzer/IRAC data sample broad swaths of the rest-frame optical for all of our sources and measures the continuum emission from older stellar populations and nebular emission lines in each lensed LAE. The Spitzer data therefore provide constraints on the strength of the Balmer jump, marginalized over the uncertainties in the strengths of the nebular emission lines.

We make use of *Prospector*'s ability to model nonparametric SFHs; we chose a nonparametric SFH with fixed time bins and a continuity prior. As described in Leja et al. (2019), this SFH setup is the best case scenario for recovering true SFHs with photometry-only SED fitting. We define eight age bins:

$$\begin{aligned} 0 < t &\leq 10 \text{ Myr}, \\ 10 < t &\leq 30 \text{ Myr}, \\ 30 < t &\leq 60 \text{ Myr}, \\ 60 < t &\leq 130 \text{ Myr}, \\ 130 < t &\leq 260 \text{ Myr}, \\ 260 < t &\leq 550 \text{ Myr}, \\ 550 \text{ Myr} < t &\leq 1.1 \text{ Gyr}, \\ 1.1 \text{ Gyr} < t &\leq t_{\text{final}} \end{aligned}$$

where  $t_{\text{final}}$  is the age of the Universe at the redshift of the LAE. Except for the first two and last age bins, the age bins are separated equally in logarithmic time, following the methodology of Leja et al. (2019). The first two bins were chosen to probe populations of very young (<10 and 10–30 Myr old) stars. Each LAE was modeled with 256 walkers and a total of 9216 MCMC iterations, excluding three preliminary “burn-in” runs.

We report three measures of the age of the stellar population: mass-weighted age,  $t_{50}$ , and  $t_{90}$ . The mass-weighted age is defined as the integral of the SFH weighted by the total amount of mass formed in each time bin.  $t_{50}$  and  $t_{90}$  are defined as the times at which the (unweighted) integral of the SFH is equal to 50% and 90% of the total stellar mass formed, respectively.

The errors on all three quantities are drawn from 1000 realizations of the SFH (1000 different walker–iteration combinations). From these distributions we report the 16th, 50th, and 84th percentiles. It is critical to note that *Prospector* calculates the stellar mass posterior distribution from image plane photometry, which is magnified by strong gravitational lensing. We calculate the intrinsic stellar mass distribution by convolving the posterior with a Gaussian distribution of the object's magnification factor.

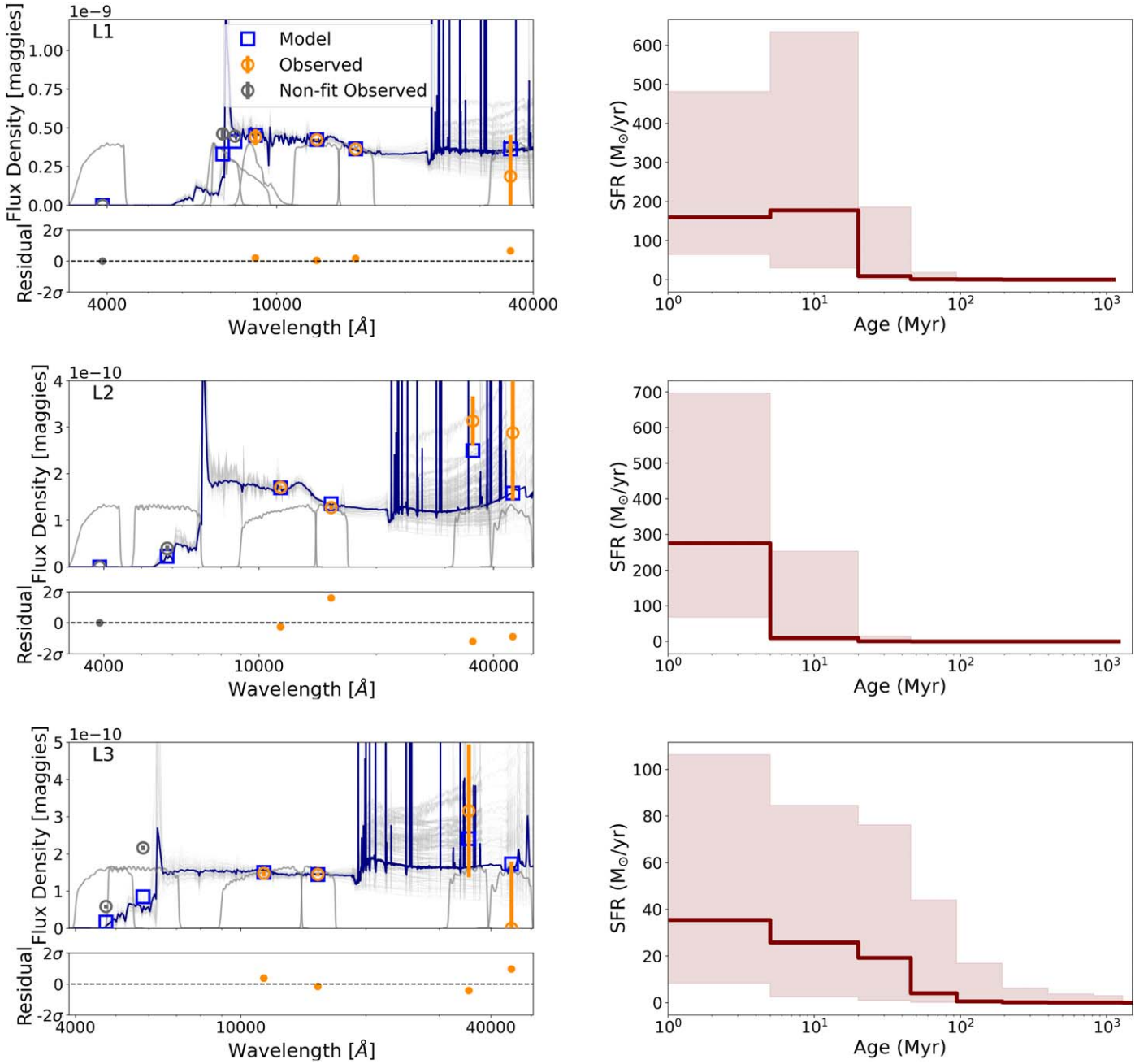


**Figure 4.** Left: SED models. The best-fit model for each LAE is shown by the dark blue curve. The gray curves behind the best-fit curve are the final 100 iterations from the end of the *emcee* chain. These approximate the spread of models *Prospector* fits to the data. Filter transmission curves for our photometry are plotted at the bottom of each plot in gray. They are shifted in wavelength space to match the redshift of the LAE and are aligned with the photometric points. Right: nonparametric star formation histories (SFHs). Age is defined as the lookback time from the time we currently see to the age of the Universe at the object’s redshift. The line and shaded regions are the 16th, 50th, and 84th percentiles of star formation rate in each age bin. The star formation rates are calculated in the image plane and are hence magnified.

### 3.3. Lens Models

Modeling the gravitational potential of the lensing system is an important aspect of analyzing strongly lensed sources. Creation of magnification maps, identification of all the images of a lensed source, and creation of source plane images through ray tracing are all examples of obtaining information only available through lens modeling. In this work we used magnification maps to calculate the intrinsic stellar mass and intrinsic Ly $\alpha$  magnitudes of our sample. We also identified previously unknown images of L1 and L5, but they were too

faint for robust analysis. We leave the use of lens models to calculate physical (source plane) sizes and distances for the subsequent paper on this sample A. Navarre et al. (2023, in preparation).

Lensing models of the systems were created using *Lenstool* (Jullo et al. 2007), which is a parametric lens-modeling software in which projected mass density halos are linearly combined. All models assumed a pseudoisothermal ellipsoidal mass distribution (PIEMD; Limousin et al. 2007) with the following parameters: position, ellipticity, position



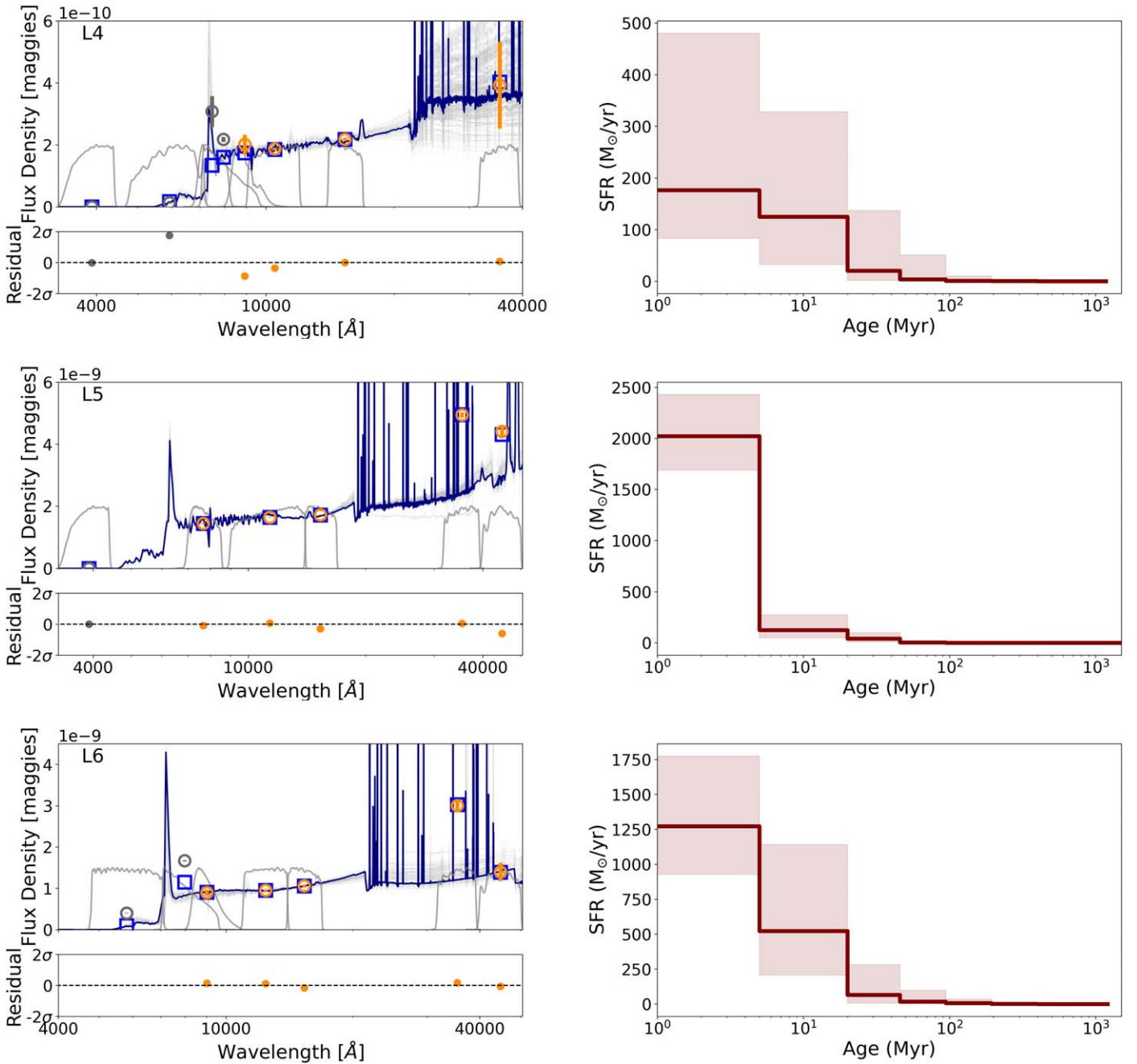


Figure 4. (Continued.)

angle, core radius, truncation radius, and normalization. The models are iteratively created, beginning with modeling the most obvious evidence of lensing, then using the output to identify additional constraints.

Lens models for L1 through L5 were computed by Sharon et al. (2020). The lens model for L6 was created for this work. All of the lens model outputs are publicly available through MAST.<sup>10</sup> Here we provide only a short summary, and refer the reader to Sharon et al. (2020) for more details. The details of the lens model of L6 will be presented in A. Navarre et al. (2023, in preparation).

### 3.4. Offset Measurements

Through visual analysis of the stellar continuum and narrowband Ly $\alpha$  imaging, we found separate bright regions within the images of L1, L2, and L5. We denote these regions with lowercase letters (L1a, L2b, etc.). Note these should not be misinterpreted as multiple images of the same object, like those found for L6. The positions of each region are shown in Table 1 and can be seen visually by the “X” symbols in Figure 3.

We calculated the on-sky offset between the stellar continuum and Ly $\alpha$  emission of each region of interest. To represent the stellar continuum, we chose the bluest filter available that contained the UV slope and did not contain Ly $\alpha$ .

<sup>10</sup> <https://archive.stsci.edu/hlsp/sgas>

We calculated the on-sky positions by using DS9’s (Joye & Mandel 2003) centroiding algorithm in each band.

### 3.5. Classification of Clumpy versus Extended

We classify the Ly $\alpha$  morphology of our LAEs in two broad categories: clumpy and extended. These classifications are derived from the spatially resolved ratio of the Ly $\alpha$  emission to the UV continuum emission. Our observations in both Ly $\alpha$  and the UV continuum are background limited, and we interpret their pixel-by-pixel ratio as something akin to an Ly $\alpha$  escape fraction map. The UV continuum is created from the same young, hot stars that create Ly $\alpha$ . Additionally, the ionizing photon emission from these stars should scale with the UV continuum. Assuming an  $f_{\text{esc,LyC}} \sim 0$ , every ionizing photon should result in approximately 0.68 Ly $\alpha$  photons (from Dijkstra 2017). In some LAEs we see both regions of high Ly $\alpha$  and low UV, and regions of low Ly $\alpha$  and high UV, surface brightness. This can be seen visually in Figure 3. We classify these LAEs as clumpy. We classify the other LAEs as extended, as their Ly $\alpha$  surface brightness scales more smoothly with the UV continuum into the circum-galactic medium.

## 4. Analysis

### 4.1. Inferred Galaxy Properties

Due to the strong lensing magnification our lensed LAE galaxies have apparent brightnesses that are among the brightest LAEs discovered in blank-field narrowband surveys of similar redshifts, but are intrinsically much fainter than typical field LAEs (Figure 5). In Table 5 we report the inferred stellar masses, ages of the stellar populations, and dust contents ( $A_V$ ). We compare our results with the following studies: Chary et al. (2005), Gawiser et al. (2006), Lai et al. (2007), Pirzkal et al. (2007), Finkelstein et al. (2009), Hayes et al. (2013), and Santos et al. (2021).

Our intrinsic stellar mass values are consistent with the other studies, which find high-redshift LAEs having stellar masses  $\sim 1 \times 10^7 M_\odot$ – $8.5 \times 10^9 M_\odot$ . Our sample probes the low-mass end of the  $z \sim 4$ – $5$  LAE mass function (Santos et al. 2021). This is unsurprising given that gravitational lensing is a rare phenomenon and low-mass LAEs are more numerous than high-mass LAEs.

Our age measurements correspond with young stellar populations, with  $t_{50} \lesssim 30$  Myr. Young stellar populations create large amounts of Ly $\alpha$ , which is consistent with their high Ly $\alpha$  EWs. The studies we compare against report ages  $\sim 5$ – $850$  Myr inferred through SED fitting. However, these values are obtained by fitting simple stellar population or exponentially decaying (tau-model) SFHs. Carnall et al. (2019) show that use of these star formation models imposes strong priors on physical parameters such as stellar population age. Our age measurements were inferred using nonparametric SFHs, which return galaxy properties with less bias and more accuracy (Leja et al. 2019). We find that the clumpy LAEs tend to be younger while the extended LAEs tend to be older, which we discuss further in Section 4.3.

We break dust attenuation into two categories: attenuation affecting young stellar populations ( $<10$  Myr, dust1) and attenuation affecting all older stellar populations ( $>10$  Myr, dust2). This distinction is based on the work of Charlot & Fall (2000). Physically, the attenuation in the birth clouds of young, massive stars can be different than the attenuation in regions

### Lensed/Intrinsic Ly $\alpha$ Luminosities vs. Field LAEs

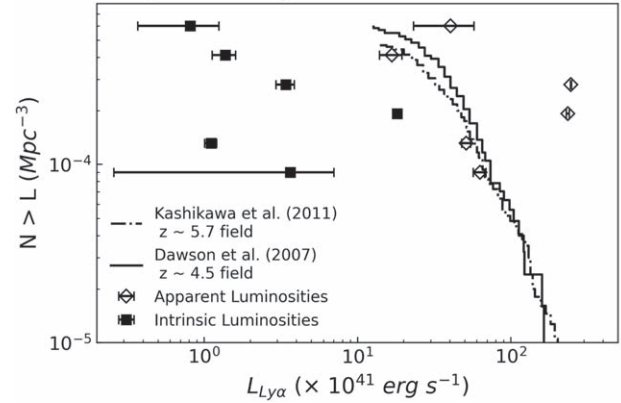


**Figure 5.** The solid and dashed lines show luminosity densities of high-redshift field LAEs from Kashikawa et al. (2011) and Dawson et al. (2007). The open diamonds are the measured Ly $\alpha$  luminosities of our sample. The filled squares are the intrinsic (delensed) luminosities, calculated from our lens model magnification maps. Note that the y-coordinates of our data points do not represent a number density. The intrinsic and observed luminosities of an LAE are placed at the same y-coordinate for clarity. Our observed luminosities are consistent with or brighter than typical field LAEs at these redshifts. The y-axis ordering of the points corresponds with L1 at the top and descends to L6 at the bottom.

where older stars have migrated away from their birth clouds. Older stellar populations may have had their surrounding gas disrupted through feedback from younger, more energetic stars. The studies to which we compare our data report dust extinctions from emission line diagnostics or SED fitting with only one dust component.

Our estimations for attenuation from young stellar populations (dust1) are consistent with these studies, with  $A_V \sim 0$ – $1$ . We find that the LAEs with extended Ly $\alpha$  morphologies have larger  $A_V$  values than those with clumpy Ly $\alpha$ . Since dust destroys Ly $\alpha$  photons, it is counterintuitive to find more in systems with extended Ly $\alpha$ . Our results imply that the main contributor to a clumpy versus extended Ly $\alpha$  morphology is the HI distribution rather than the amount of dust.

### 4.2. Ly $\alpha$ and UV Spatial Coincidence

The measured image plane spatial separation between the Ly $\alpha$  centroid and stellar continuum is reported in Table 6 as  $\delta_{\text{Ly}\alpha}$ . Studies measuring large samples of field LAEs indicate that a significant portion contain a spatial offset. Jiang et al. (2013) found that there is little offset between the UV and Ly $\alpha$  positions in compact galaxies ( $<0''.2$ ), but merging/interacting systems can be significantly offset ( $>0''.3$ ). Shibuya et al. (2014) found the majority of their LAE sample is offset by  $<0''.2$ , yet only  $\approx 23\%$  are classified as mergers. Our measurements do not take into account the distortion from gravitational lensing and should be considered upper limits to the true (source plane) separations. We find that all of the Ly $\alpha$  regions studied in our sample have small offsets  $<0''.2$ , indicating that they are likely not merging or interacting galaxies.

### 4.3. Ly $\alpha$ Morphology

Robust quantitative descriptions of the Ly $\alpha$  morphology require forward modeling through the lensing potential, and is left to the follow-up paper (A. Navarre et al. 2023, in preparation). Here we present a qualitative discussion of the

**Table 5**  
Table of Inferred Galaxy Properties from *Prospector*

ID	Ly $\alpha$ Morphology	log(Stellar Mass) ( $M_{\odot}$ ) (Lensed)	log(Stellar Mass) ( $M_{\odot}$ ) (Intrinsic)	Mass-weighted Age (Myr)	$t_{50}$ (Myr)	$t_{90}$ (Myr)	Dust1 ( $A_V$ )	Dust2 ( $A_V$ )
L1	Clumpy	$9.85^{+0.62}_{-0.48}$	$8.15^{+0.64}_{-0.51}$	$17^{+19}_{-8}$	$13^{+14}_{-7}$	$44^{+510}_{-25}$	$0.10^{+0.23}_{-0.08}$	$0.82^{+0.92}_{-0.69}$
L2	Clumpy	$9.72^{+0.43}_{-0.61}$	$8.60^{+0.44}_{-0.61}$	$8^{+9}_{-3}$	$4^{+11}_{-1}$	$18^{+220}_{-13}$	$0.09^{+0.14}_{-0.07}$	$2.15^{+0.64}_{-1.30}$
L3	Extended	$9.69^{+0.58}_{-0.68}$	$7.79^{+0.58}_{-0.68}$	$33^{+83}_{-20}$	$38^{+230}_{-26}$	$187^{+850}_{-150}$	$0.57^{+0.84}_{-0.43}$	$0.35^{+0.75}_{-0.29}$
L4	Extended	$9.94^{+0.45}_{-0.40}$	$8.82^{+0.45}_{-0.40}$	$20^{+27}_{-9}$	$17^{+41}_{-7}$	$87^{+580}_{-68}$	$0.46^{+0.47}_{-0.28}$	$0.54^{+0.69}_{-0.39}$
L5	Clumpy	$10.41^{+0.09}_{-0.08}$	$8.71^{+0.10}_{-0.10}$	$7^{+2}_{-1}$	$4^{+1}_{-1}$	$33^{+12}_{-18}$	$0.23^{+0.06}_{-0.06}$	$1.00^{+0.16}_{-0.15}$
L6	Extended	$10.55^{+0.26}_{-0.26}$	$9.24^{+0.47}_{-0.37}$	$16^{+11}_{-06}$	$14^{+26}_{-6}$	$130^{+490}_{-110}$	$0.42^{+0.56}_{-0.31}$	$0.80^{+0.39}_{-0.44}$

**Note.** The associated SEDs are found in Figure 4 and correspond with the above quantities. Dust is broken into two components: dust1 and dust2. These are defined as the amount of dust attenuation affecting stars with ages  $< 10$  Myr (dust1) and  $> 10$  Myr (dust2). This distinction is based on the work of Charlot & Fall (2000), where the environments of young and old stellar populations contain different amounts of dust (see Section 4.1). We report three measures of the age: mass-weighted age,  $t_{50}$ , and  $t_{90}$ , as defined in Section 3.2. We include the Ly $\alpha$  morphology classification (see Section 4.3) for reference.

**Table 6**  
Image-plane (On-sky) Angular Offsets between the Stellar Continuum and Ly $\alpha$  Emission

ID	Image Plane $\delta_{\text{Ly}\alpha}$ (")	Stellar Continuum Band
L1a	0.090	F125W
L1b	0.042	F125W
L2a	0.067	F110W
L2b	0.030	F110W
L3	0.060	F110W
L4	0.042	F105W
L5	0.030	F775W
L6'	0.095	F850LP
L6''	0.108	F850LP
L6'''	0.095	F850LP

**Note.** We list the filters used for the stellar continuum, which were chosen as the bluest available filters redward of Ly $\alpha$  that did not contain Ly $\alpha$ . Since our measurements are not corrected for distortion from gravitational lensing, our findings should be considered as upper limits to the intrinsic (source plane) separation.

morphologies. One can see in Figure 3 that the Ly $\alpha$  contours fall into two broad categories: extended and clumpy. L1, L2, and L5 have clumpy Ly $\alpha$  morphologies: the Ly $\alpha$  emission does not cover the entire galaxy, and instead is concentrated in specific regions. L3, L4, and L6 have extended morphologies: their Ly $\alpha$  emission covers the entire galaxy and extends beyond the associated stellar continuum emission. This broadening is consistent with Ly $\alpha$  radiative transfer.

We propose that our LAEs containing clumpy Ly $\alpha$  morphologies have varying HI column densities across their star-forming regions. Since HI scatters Ly $\alpha$ , lines of sight with lower HI column densities preferentially allow more Ly $\alpha$  photons to escape. The Ly $\alpha$  clumps seen in our sample could align with these lines of sight. This hypothesis is supported by previous observations of Ly $\alpha$ -emitting galaxies with evidence of nonuniform HI distributions (Heckman et al. 2011; Rivera-Thorsen et al. 2017; Chisholm et al. 2018; Gazagnes et al. 2018; Steidel et al. 2018). Furthermore, simulations of a similar galaxy in Blaizot et al. (2023) find significant anisotropic effects on the Ly $\alpha$  line shape and luminosity. These effects correlate with gas flows and evolve over short timescales ( $\sim$ tens of megayears), implying the possibility of short-lived gas configurations that can create clumpy Ly $\alpha$  morphologies.

Our sample suggests a progression from clumpy Ly $\alpha$  to extended Ly $\alpha$  over a timescale of  $\sim 14$ – $38$  Myr based on  $t_{50}$ .

The clumpy LAEs tend to be younger while the extended LAEs tend to be older. We note that L1 and L6 have similar ages while being classified differently, and explain this through our SFH resolution. Our first three SFH age bins cover (0,10] Myr, (10,30] Myr, and (30,61.7] Myr, respectively. The upper error in  $t_{50}$  of L6 is larger than that of L1, extending beyond 30 Myr while L1 does not. This implies that the stellar population of L6 contains more older stars than that of L1. Due to the errors on the ages and our small sample size we do not claim that this observation is robust; instead it is merely suggestive.

A possible explanation of this apparent difference is that clumpy Ly $\alpha$  morphologies appear in a short-lived stage of starbursts. In this initial stage young massive stars ionize channels along preferential lines of sight. As more stars are formed and greater densities of ionizing photons are created, more lines of sight are punched through the interstellar medium. These ionized channels allow Ly $\alpha$  to directly escape the LAE more easily through them into the intergalactic medium (IGM), explaining the presence of the clumpy Ly $\alpha$  morphologies. It is also possible that the inflowing gas that fuels bursts of star formation obscures lines of sight that would otherwise leak Ly $\alpha$  (Blaizot et al. 2023). However, not all Ly $\alpha$  that escapes a star-forming region necessarily immediately exits into the IGM. Ionized channels allow Ly $\alpha$  to escape into the extended halo of neutral hydrogen that surrounds the LAE, where it can then scatter into an extended profile.

## 5. Summary

We have investigated the image plane properties of six Ly $\alpha$ -emitting galaxies at  $4.1 < z < 5.2$ . Using multiband imaging from HST and Spitzer, we were able to infer stellar masses, ages, and  $A_V$  values with *Prospector*. Taking advantage of magnification from gravitational lensing and HST-resolution narrowband filters we were able to measure Ly $\alpha$  on subgalactic scales otherwise inaccessible. With the HST narrowband Ly $\alpha$  imaging we were able to see different types of Ly $\alpha$  morphology: clumpy versus extended. Through use of lens models we were able to calculate the intrinsic stellar masses and Ly $\alpha$  luminosities. Our findings are summarized below.

1. The intrinsic stellar masses, ages, and amounts of dust are consistent with values from other studies of high- and low-redshift LAEs. In particular, the young ages of the stellar populations are consistent with the kinds of stars that produce high amounts of Ly $\alpha$ .



2. The offsets between the stellar continuum and Ly $\alpha$  emission of our sample are small ( $<0.2$ ). This is consistent with other studies which find small spatial offsets, and can be explained through radiative transfer through nonuniform H I distributions. The small offsets indicate our LAEs are not interacting or merging systems.
3. A qualitative analysis of the Ly $\alpha$  emission shows two broad categories of Ly $\alpha$  morphologies: clumpy and extended. We find that the LAEs containing clumpy Ly $\alpha$  generally have younger stellar populations. This suggests a possible progression from clumpy Ly $\alpha$  to extended Ly $\alpha$ , perhaps driven by the growth of young massive stars and the creation of ionized channels during a starburst period.

Future work (A. Navarre et al. 2023, in preparation) will further study the source plane (intrinsic) morphologies of this sample. That work will include state-of-the-art custom forward modeling code to measure the sizes and distances robustly through the lensing potential. That work will measure the physical sizes of the Ly $\alpha$  regions, stellar continuum regions, and Ly $\alpha$  offsets; reconstruct the source plane images of the LAEs; and detail the new lens model for L6. We will directly compare the physical information with samples of low- and high-redshift LAEs, as well as with the inferred galaxy properties from this paper. We will characterize the variations in the morphology of the Ly $\alpha$  emission and compare them to low-redshift LAEs, where the distribution of Ly $\alpha$  is heterogeneous (Bond et al. 2010; Finkelstein et al. 2011; Steidel et al. 2011; Feldmeier et al. 2013; Momose et al. 2014).

### Acknowledgments

Support for HST program HST-GO-13639 was provided by NASA through a grant from the Space Telescope Science Institute, which is operated by the Association of Universities for Research in Astronomy, Inc., under NASA contract NAS 5-26555.

Based on observations made with the NASA/ESA Hubble Space Telescope, obtained at the Space Telescope Science Institute, which is operated by the Association of Universities for Research in Astronomy, Inc., under NASA contract NAS 5-26555. These observations are associated with programs HST-GO-9135, HST-GO-11974, HST-GO-13003, HST-GO-13639, and HST-GO-14497.

This work is based in part on observations made with the Spitzer Space Telescope, which was operated by the Jet Propulsion Laboratory, California Institute of Technology under a contract with NASA. Support for the Spitzer programs used in this work was provided by NASA. Spitzer data used in this analysis were taken as a part of programs #20754, #60158, #70154, and #90232.

Some of the data presented in this paper were obtained from the Mikulski Archive for Space Telescopes (MAST): doi:10.17909/jvg9-v026.

### ORCID iDs

Alexander Navarre  <https://orcid.org/0000-0001-7548-0473>  
 Gourav Khullar  <https://orcid.org/0000-0002-3475-7648>  
 Matthew B. Bayliss  <https://orcid.org/0000-0003-1074-4807>  
 Håkon Dahle  <https://orcid.org/0000-0003-2200-5606>  
 Michael Florian  <https://orcid.org/0000-0001-5097-6755>  
 Michael Gladders  <https://orcid.org/0000-0003-1370-5010>

Keunho J. Kim  <https://orcid.org/0000-0001-6505-0293>  
 M. Riley Owens  <https://orcid.org/0000-0002-2862-307X>  
 Jane Rigby  <https://orcid.org/0000-0002-7627-6551>  
 Joshua Roberson  <https://orcid.org/0000-0002-0975-623X>  
 Keren Sharon  <https://orcid.org/0000-0002-7559-0864>  
 Ryan Walker  <https://orcid.org/0000-0001-5424-3698>

### References

- Atek, H., Labbé, I., Furtak, L. J., et al. 2023, arXiv:2308.08540
- Bayliss, M. B., Hennawi, J. F., Gladders, M. D., et al. 2011, *ApJS*, 193, 8
- Bayliss, M. B., Rigby, J. R., Sharon, K., et al. 2014, *ApJ*, 790, 144
- Bayliss, M. B., Wuyts, E., Sharon, K., et al. 2010, *ApJ*, 720, 1559
- Berg, D. A., Erb, D. K., Auger, M. W., Pettini, M., & Brammer, G. B. 2018, *ApJ*, 859, 164
- Bertin, E., & Arnouts, S. 1996, *A&AS*, 117, 393
- Blaizot, J., Garel, T., Verhamme, A., et al. 2023, *MNRAS*, 523, 3749
- Bond, N. A., Feldmeier, J. J., Matković, A., et al. 2010, *ApJL*, 716, L200
- Carnall, A. C., Leja, J., Johnson, B. D., et al. 2019, *ApJ*, 873, 44
- Charlot, S., & Fall, S. M. 2000, *ApJ*, 539, 718
- Chary, R.-R., Stern, D., & Eisenhardt, P. 2005, *ApJL*, 635, L5
- Chisholm, J., Gazagnes, S., Schaerer, D., et al. 2018, *A&A*, 616, A30
- Conroy, C., & Gunn, J. E. 2010, *ApJ*, 712, 833
- Conroy, C., Gunn, J. E., & White, M. 2009, *ApJ*, 699, 486
- Cowie, L. L., Barger, A. J., & Hu, E. M. 2011, *ApJ*, 738, 136
- Cowie, L. L., & Hu, E. M. 1998, *AJ*, 115, 1319
- Dawson, S., Rhoads, J. E., Malhotra, S., et al. 2007, *ApJ*, 671, 1227
- Deharveng, J.-M., Small, T., Barlow, T. A., et al. 2008, *ApJ*, 680, 1072
- Dijkstra, M. 2017, Saas-Fee Lecture Notes: Physics of Ly $\alpha$  Radiative Transfer, arXiv:1704.03416
- Dressler, A., Martin, C. L., Henry, A., Sawicki, M., & McCarthy, P. 2011, *ApJ*, 740, 71
- Erb, D. K., Berg, D. A., Auger, M. W., et al. 2019, *ApJ*, 884, 7
- Feldmeier, J. J., Hagen, A., Ciardullo, R., et al. 2013, *ApJ*, 776, 75
- Finkelstein, S. L., Cohen, S. H., Windhorst, R. A., et al. 2011, *ApJ*, 735, 5
- Finkelstein, S. L., Malhotra, S., Rhoads, J. E., Hathi, N. P., & Pirzkal, N. 2009, *MNRAS*, 393, 1174
- Finkelstein, S. L., Rhoads, J. E., Malhotra, S., Grogan, N., & Wang, J. 2008, *ApJ*, 678, 655
- Florian, M. K., Rigby, J. R., Acharyya, A., et al. 2021, *ApJ*, 916, 50
- Foreman-Mackey, D., Hogg, D. W., Lang, D., & Goodman, J. 2013, *PASP*, 125, 306
- Gawiser, E., van Dokkum, P. G., Gronwall, C., et al. 2006, *ApJL*, 642, L13
- Gazagnes, S., Chisholm, J., Schaerer, D., et al. 2018, *A&A*, 616, A29
- Gladders, M. D., Hoekstra, H., Yee, H. K. C., Hall, P. B., & Barrientos, L. F. 2003, *ApJ*, 593, 48
- Gladders, M. D., Yee, H. K. C., & Ellingson, E. 2002, *AJ*, 123, 1
- Gonzaga, S., Hack, W., Fruchter, A., & Mack, J. 2012, *The DrizzlePac Handbook*
- Gronwall, C., Ciardullo, R., Hickey, T., et al. 2007, *ApJ*, 667, 79
- Guaita, L., Acquaviva, V., Padilla, N., et al. 2011, *ApJ*, 733, 114
- Hayes, M., Östlin, G., Schaerer, D., et al. 2013, *ApJL*, 765, L27
- Hekman, T. M., Borthakur, S., Overzier, R., et al. 2011, *ApJ*, 730, 5
- Henry, A., Scarlata, C., Martin, C. L., & Erb, D. 2015, *ApJ*, 809, 19
- Herrero Alonso, Y., Wisotzki, L., Miyaji, T., et al. 2023, *A&A*, 677, A125
- Jiang, L., Egami, E., Fan, X., et al. 2013, *ApJ*, 773, 153
- Johnson, B. D., Leja, J., Conroy, C., & Speagle, J. S. 2021, *ApJS*, 254, 22
- Joye, W. A., & Mandel, E. 2003, in ASP Conf. Ser. 295, *Astronomical Data Analysis Software and Systems XII*, ed. H. E. Payne, R. I. Jedrzejewski, & R. N. Hook (San Francisco, CA: ASP), 489
- Jullo, E., Kneib, J.-P., Limousin, M., et al. 2007, *NJPh*, 9, 447
- Jung, I., Finkelstein, S. L., Arrabal Haro, P., et al. 2023, arXiv:2304.05385
- Kashikawa, N., Shimasaku, K., Matsuda, Y., et al. 2011, *ApJ*, 734, 119
- Kikuta, S., Ouchi, M., Shibuya, T., et al. 2023, *ApJS*, 268, 24
- Lai, K., Huang, J.-S., Fazio, G., et al. 2007, *ApJ*, 655, 704
- Leja, J., Carnall, A. C., Johnson, B. D., Conroy, C., & Speagle, J. S. 2019, *ApJ*, 876, 3
- Limousin, M., Richard, J., Jullo, E., et al. 2007, *ApJ*, 668, 643
- Marques-Chaves, R., Pérez-Fourmon, I., Shu, Y., et al. 2017, *ApJL*, 834, L18
- Momose, R., Ouchi, M., Nakajima, K., et al. 2014, *MNRAS*, 442, 110
- Mukae, S., Ouchi, M., Hill, G. J., et al. 2020, *ApJ*, 903, 24
- Navarre, A. 2023a, Replication HST Narrowband Data for: Resolving Clumpy vs. Extended Ly- $\alpha$  In Strongly Lensed, High-Redshift Ly- $\alpha$  Emitters Harvard Dataverse, doi:10.7910/DVN/9QOYYW

- Navarre, A. 2023b, Replication Spitzer Data for: Resolving Clumpy vs. Extended Ly $\alpha$  In Strongly Lensed, High-Redshift Ly- $\alpha$  Emitters Harvard Dataverse, doi:[10.7910/DVN/JSVGM8](https://doi.org/10.7910/DVN/JSVGM8)
- Ono, Y., Shimasaku, K., Dunlop, J., et al. 2010, *ApJ*, **724**, 1524
- Östlin, G., Hayes, M., Duval, F., et al. 2014, *ApJ*, **797**, 11
- Östlin, G., Hayes, M., Kunth, D., et al. 2009, *AJ*, **138**, 923
- Ouchi, M., Shimasaku, K., Akiyama, M., et al. 2008, *ApJS*, **176**, 301
- Peng, C. Y., Ho, L. C., Impey, C. D., & Rix, H.-W. 2010, *AJ*, **139**, 2097
- Pirzkal, N., Malhotra, S., Rhoads, J. E., & Xu, C. 2007, *ApJ*, **667**, 49
- Rhoads, J. E., Malhotra, S., Dey, A., et al. 2000, *ApJL*, **545**, L85
- Rivera-Thorsen, T. E., Dahle, H., Gronke, M., et al. 2017, *A&A*, **608**, L4
- Rzepecki, J., Lombardi, M., Rosati, P., Bignamini, A., & Tozzi, P. 2007, *A&A*, **471**, 743
- Saldana-Lopez, A., Schaerer, D., Chisholm, J., et al. 2023, *MNRAS*, **522**, 6295
- Santos, S., Sobral, D., Butterworth, J., et al. 2021, *MNRAS*, **505**, 1117
- Scarlata, C., Colbert, J., Teplitz, H. I., et al. 2009, *ApJL*, **704**, L98
- Sharon, K. 2022, SDSS Giant Arcs Survey (“SGAS”), STScI/MAST, doi:[10.17909/T9-CQTJ-Y020](https://doi.org/10.17909/T9-CQTJ-Y020)
- Sharon, K., Bayliss, M. B., Dahle, H., et al. 2020, *ApJS*, **247**, 12
- Shibuya, T., Ouchi, M., Nakajima, K., et al. 2014, *ApJ*, **785**, 64
- Smit, R., Swinbank, A. M., Massey, R., et al. 2017, *MNRAS*, **467**, 3306
- Steidel, C. C., Bogosavljević, M., Shapley, A. E., et al. 2011, *ApJ*, **736**, 160
- Steidel, C. C., Bogosavljević, M., Shapley, A. E., et al. 2018, *ApJ*, **869**, 123
- Swinbank, A. M., Bower, R. G., Smith, G. P., et al. 2007, *MNRAS*, **376**, 479
- Thai, T. T., Tuan-Anh, P., Pello, R., et al. 2023, *A&A*, **678**, A139
- Verhamme, A., Garel, T., Ventou, E., et al. 2018, *MNRAS*, **478**, L60
- Witstok, J., Smit, R., Maiolino, R., et al. 2021, *MNRAS*, **508**, 1686
- Witstok, J., Smit, R., Saxena, A., et al. 2024, *A&A*, **682**, A40
- Yamada, S. F., Sasaki, S. S., Sumiya, R., et al. 2005, *PASJ*, **57**, 881
- York, D. G., Adelman, J., Anderson, J. E. J., et al. 2000, *AJ*, **120**, 1579